

Does Concentration Drive the Scatter in the Stellar-to-Halo Mass Relation of Galaxy Clusters?

Ying Zu^{1,2*}, Huanyuan Shan³, Jun Zhang^{1,2}, Sukhdeep Singh⁴, Zhiwei Shao¹, Xiaokai Chen¹, Ji Yao¹, Jesse B. Golden-Marx¹, Weiguang Cui⁵, Eric Jullo⁶, Jean-Paul Kneib^{6,7}, Pengjie Zhang^{1,2}, Xiaohu Yang^{1,2}

¹Department of Astronomy, School of Physics and Astronomy, Shanghai Jiao Tong University, Shanghai 200240, China

²Shanghai Key Laboratory for Particle Physics and Cosmology, Shanghai Jiao Tong University, Shanghai 200240, China

³Key Laboratory for Research in Galaxies and Cosmology, Shanghai Astronomical Observatory, Shanghai 200030, China

⁴McWilliams Center for Cosmology, Department of Physics, Carnegie Mellon University, 5000 Forbes Avenue, Pittsburgh, PA 15213, USA

⁵Institute for Astronomy, University of Edinburgh, Royal Observatory, Edinburgh EH9 3HJ, United Kingdom

⁶Aix-Marseille Univ, CNRS, CNES, LAM, Marseille, France

⁷Institute of Physics, Laboratory of Astrophysics, Ecole Polytechnique Fédérale de Lausanne (EPFL), Observatoire de Sauverny, 1290 Versoix, Switzerland

Accepted XXX. Received YYY; in original form ZZZ

ABSTRACT

Concentration is one of the key dark matter halo properties that could drive the scatter in the stellar-to-halo mass relation of massive clusters. We derive robust photometric stellar masses for a sample of brightest central galaxies (BCGs) in SDSS redMaPPer clusters at $0.17 < z < 0.3$, and split the clusters into two equal-halo mass subsamples by their BCG stellar mass M_*^{BCG} . The weak lensing profiles $\Delta\Sigma$ of the two cluster subsamples exhibit different slopes on scales below $1h^{-1}\text{Mpc}$. To interpret such discrepancy, we perform a comprehensive Bayesian modelling of the two $\Delta\Sigma$ profiles by including different levels of miscentring effects between the two subsamples as informed by X-ray observations. We find that the two subsamples have the same average halo mass of $1.74 \times 10^{14} h^{-1} M_\odot$, but the concentration of the low- M_*^{BCG} clusters is $5.87^{+0.77}_{-0.60}$, $\sim 1.5\sigma$ smaller than that of their high- M_*^{BCG} counterparts ($6.95^{+0.78}_{-0.66}$). Furthermore, both cluster weak lensing and cluster-galaxy cross-correlations indicate that the large-scale bias of the low- M_*^{BCG} , low-concentration clusters are $\sim 10\%$ higher than that of the high- M_*^{BCG} , high-concentration systems, hence possible evidence of the cluster assembly bias effect. Our results reveal a remarkable physical connection between the stellar mass within $20\text{--}30h^{-1}\text{kpc}$, the dark matter mass within $\sim 200h^{-1}\text{kpc}$, and the cosmic overdensity on scales above $10h^{-1}\text{Mpc}$, enabling a key observational test of theories of co-evolution between massive clusters and their central galaxies.

Key words: galaxies: formation — cosmology: large-scale structure of Universe — gravitational lensing: weak

1 INTRODUCTION

As the most dominant galaxies at the center of massive clusters (Kravtsov & Borgani 2012; Von Der Linden et al. 2007), the brightest central galaxies (BCGs¹) have witnessed both the early-time fast growth and the late-time slow accretion of cluster haloes predicted by hierarchical structure formation in the ΛCDM Universe (Zhao et al. 2003; Klypin et al. 2016). Consequently, the BCGs have likely experienced an analogous two-phase formation,

with starbursts induced by gas-rich mergers (Barnes & Hernquist 1991; Mihos & Hernquist 1996; Hopkins et al. 2013) and fast accretion (Fabian 1994; Collins et al. 2009; McDonald et al. 2012) at the onset of cluster formation, followed by dry mergers and smooth accretions until the observed epoch (Lin & Mohr 2004; Bezanson et al. 2009; van Dokkum et al. 2010; Zhang et al. 2016; Huang et al. 2018; DeMaio et al. 2020). The correlated growth of cluster haloes and BCGs is also seen in numerical simulations of cluster formation (Dubinski 1998; Mostoghiu et al. 2019; Ragagnin et al. 2019; Rennehan et al. 2020). Therefore, the scatter in the stellar-to-halo mass relation of BCGs inevitably carries the imprint of the assembly history of cluster haloes, providing an important avenue to the physical understanding of galaxy-halo connection at the very

* E-mail: yingzu@sjtu.edu.cn

¹ We use BCGs to refer to the brightest central or brightest cluster galaxies interchangeably.

massive end (Wechsler & Tinker 2018). In this paper, we measure the weak gravitational lensing signals of two equal-halo mass cluster subsamples split by BCG stellar mass, and look for possible discrepancies in their halo concentration c , one of the most fundamental halo properties that correlates strongly with halo assembly history.

The mean concentration of haloes declines slowly with mass in the cluster regime (Jing & Suto 2000; Wang et al. 2020b), with a hint of an upturn at the highest mass end (Klypin et al. 2011; Prada et al. 2012). Using the extended Press-Schechter formalism (Bond et al. 1991; Bower 1991; Lacey & Cole 1993), Navarro et al. (1997) was the first to suggest that c is linked to the formation time of haloes. Since then, the physical connection between the $c - M_h$ relation and the average mass assembly history (MAH) of haloes has been the subject of extensive study (Bullock et al. 2001; Wechsler et al. 2002; Zhao et al. 2009; Ludlow et al. 2013; Diemer & Kravtsov 2015; Ishiyama et al. 2020). For example, Salvador-Solé et al. (1998) found that the scale radius of haloes is essentially proportional to their virial radius at the time of formation. Zhao et al. (2003) found that the MAH generally consists of an early phase of fast accretion when c stays roughly constant and a late phase of slow accretion when c increases with time, separated at a time when $c \sim 4$ and the typical binding energy of the halo is approximately equal to that of a singular isothermal sphere with the same circular velocity.

However, haloes at fixed mass have significant scatter in their concentration values (Jing & Suto 2000), and many studies have attempted to identify the key parameter that causes individual haloes to deviate from the mean $c - M_h$ relation. Mergers strongly perturb individual halo formation histories from the average MAH, but they mostly contribute to the variance of concentration at fixed formation time and halo mass (Rey et al. 2019; Wang et al. 2020a; Chen et al. 2020). Applying the secondary infall model (Gunn & Gott 1972; Fillmore & Goldreich 1984; Bertschinger 1985) to the initial Lagrangian region around cluster-size haloes, Ascasibar et al. (2007) argued that the diversity in halo concentration arises from the scatter in the primordial spherically average density profile rather than in the angular momentum distribution of dark matter. Building on the insight from the peak background split theory (Mo & White 1996; Sheth & Tormen 1999), Dalal et al. (2008) proposed that the most important parameter is the curvature of the rare density peaks in the initial Gaussian random field, so that highly curved peaks produce more concentrated haloes. In a similar vein, Diemer & Kravtsov (2015) found that the deviations can be explained by the residual dependence of c on the local slope of the matter power spectrum. Therefore, the scatter of concentration at fixed mass is largely driven by the diversity of the local environments of the initial Lagrangian peaks (including geometric environments; see Hellwing et al. 2020).

It is possible that the deviations of cluster haloes from the mean $c - M_h$ relation translate at least partly into the scatter in the stellar-to-halo mass relation (SHMR) of the BCGs. Through starbursts induced by major mergers and rapid accretion, the early growth of the BCGs at fixed halo mass should depend critically on the strength of the potential well in the inner region of clusters, which was already set before the scale radius (defined as halo radius over c) was stabilized (van den Bosch 2017). Therefore, the initial scatter in BCG stellar mass should be tightly correlated with the MAH of haloes, hence concentration. In the presence of strong Active Galactic Nuclei (AGN) feedbacks (Martizzi et al. 2012; Cui et al. 2018), the BCG *in-situ* stellar growth due to star formation would be quenched while the halo mass (and the *ex-situ* component of BCG stellar mass) continues to grow, weakening the correlation

between BCG stellar mass and halo concentration. However, AGN feedback is linked to the growth history of the supermassive black hole (SMBH), which could also be correlated with concentration at fixed halo mass, in a similar spirit to the $M_{\text{BH}} - \sigma$ relation (Gebhardt et al. 2000; Ferrarese & Merritt 2000; Gültekin et al. 2009). Indeed, hydro-simulations and semi-analytic models that turn on AGN feedback in galaxy formation generally predict that the scatter in SHMR is tied to halo formation time or concentration, albeit with large uncertainties in the cluster mass range (Wang et al. 2013; Matthee et al. 2017; Tojeiro et al. 2017; Artale et al. 2018; Zehavi et al. 2019; Bose et al. 2019). Conversely, the redistribution of binding energy between dark matter and baryons during BCG formation may slightly increase the halo concentration (Rudd et al. 2008).

The observed scatter in the SHMR of clusters is generally believed to be ≤ 0.2 dex. For example, Kravtsov et al. (2018) measured the scatter to be ~ 0.2 dex from 21 X-ray clusters with individual halo mass estimated from X-ray observations (Kravtsov et al. 2006). Zu & Mandelbaum (2015) detected a weak decreasing trend of scatter from 0.22 dex in L_* -galaxies to 0.18 dex in the cluster regime. Finding the physical driver for such a small scatter requires a large volume-limited sample of clusters with accurate measurements of halo mass and concentration, which can then be divided into subsamples of different average BCG stellar masses at fixed halo mass (but see Golden-Marx & Miller 2018, 2019, for unbinned statistical methods). This has recently become possible with the advent of large optical cluster samples detected from all-sky imaging surveys (Kochanek et al. 2003; Koester et al. 2007; Szabo et al. 2011; Wen et al. 2012; Rykoff et al. 2014; Oguri et al. 2018). In particular, we will employ the volume-limited redMaPPer cluster (v6.3) catalogue derived from the SDSS DR8 photometry (Rykoff et al. 2014), and measure the average halo mass and concentration from the stacked weak gravitational lensing profiles of clusters.

This paper is organized as follows. We describe the cluster catalogue, BCG stellar mass estimates, and weak lensing measurements in §2. The theoretical model of weak lensing signals and the Bayesian inference method are described in §3. We present our model constraints on halo mass, concentration, and bias in §4 and provide further measurement of halo bias from cluster-galaxy cross-correlations in §5. An apparent conundrum on the SHMR at fixed satellite richness is discussed in §6 before we conclude by summarising our results and look to the future in §7.

Throughout this paper, we assume the *Planck* cosmology (Planck Collaboration et al. 2020). All the length and mass units in this paper are scaled as if the Hubble constant is $100 \text{ km s}^{-1} \text{ Mpc}^{-1}$. In particular, all the separations are co-moving distances in units of $h^{-1} \text{ Mpc}$, and the halo and stellar mass are in units of $h^{-1} M_{\odot}$ and $h^{-2} M_{\odot}$, respectively. We use $\lg x = \log_{10} x$ for the base-10 logarithm and $\ln x = \log_e x$ for the natural logarithm.

2 DATA AND MEASUREMENTS

2.1 Cluster Catalogue

We employ the optical cluster catalogue derived from SDSS DR8 (York et al. 2000; Aihara et al. 2011) imaging using the red-sequence-based matched-filter photometric cluster finding algorithm redMaPPer (Rykoff et al. 2014). For each cluster, the redMaPPer algorithm measures a richness λ as its proxy for halo mass, which corresponds roughly to the number of satellite galaxies brighter than $0.2 L_*$ within an aperture $\sim 1 h^{-1} \text{ Mpc}$ (with a weak dependence on

λ). At $\lambda \geq 20$, the SDSS redMaPPer cluster catalogue is approximately volume-complete up to $z \approx 0.33$, with cluster photometric redshift uncertainties as small as $\delta(z) = 0.006/(1+z)$ (Rykoff et al. 2014; Rozo et al. 2015). More important, the log-normal scatter of λ at fixed halo mass is as small as 0.2–0.25 dex, providing an excellent halo mass proxy for our analysis (Simet et al. 2017; Murata et al. 2018; Costanzi et al. 2019).

To ensure that the cluster sample is volume-complete, we select the 4567 BCGs in the redMaPPer $\lambda > 20$ clusters between $z = 0.17$ – 0.30 ($\langle z \rangle = 0.242$), within the same redshift range of the BOSS LOWZ spectroscopic galaxy sample. Those BCGs are identified by the redMaPPer algorithm as the most likely central galaxies of the clusters. Among the 4567 BCGs, 957 of them (21 per cent) do not have spectroscopic coverage from SDSS, hence no spectroscopic stellar mass measurements from, e.g., Chen et al. (2012). Unfortunately, those 957 BCGs are preferentially systems with stellar mass (as will be estimated later with from broad-band photometry in § 2.2) below $10^{11} h^{-2} M_{\odot}$ and above $3 \times 10^{11} h^{-2} M_{\odot}$ — they are the either the lowest or the highest- M_{*}^{BCG} galaxies at fixed λ (Zu 2020). This spectroscopic incompleteness significantly reduces our capability of resolving the full range of scatter in the cluster SHMR. Additionally, the selection of the BOSS LOWZ galaxies relies on a complex set of colour cuts (Reid et al. 2016), which further complicates the selection function of our otherwise volume-completed cluster sample. To circumvent the spectroscopic stellar mass-incompleteness issue, we choose to re-measure the stellar masses for all 4567 BCGs using photometry. Thanks to the accurate cluster photo- z estimates, we are able to derive the stellar masses with reasonable accuracy from SDSS broad-band photometry in the next Section.

2.2 Stellar Mass of the Brightest Central Galaxies

Adopting the redMaPPer cluster photometric redshifts for the BCGs, we derive stellar masses for all 4567 BCGs by fitting a two-component Simple Stellar Population (SSP) template to their SDSS *gri* photometry. Following Maraston et al. (2009), we assume the dominant stellar population (97 per cent) to be solar metallicity and include a secondary (3 per cent) metal-poor ($Z=0.008$) population with the same age. We utilize the EzGal software (Mancone & Gonzalez 2012) and adopt the Bruzual & Charlot (2003) SSP model and the Chabrier (2003) IMF for the fits. We carry out the fit on extinction-corrected model magnitudes that are scaled to the *i*-band *c*-model magnitudes. This scaling assumes the outer parts of galaxy profiles are strictly de Vaucouleurs, which is adequate for isolated elliptical galaxies, but could underestimate the stellar mass for BCGs by a factor of 2–4 (Bernardi et al. 2013; Kravtsov et al. 2018). Therefore, our stellar mass estimates should be regarded as the mass of the interior or *in-situ* component of the BCGs. The total BCG+ICL (intra-cluster light) profiles of the same clusters will be presented in Chen et al. (in prep).

Figure 1 shows the comparison between the BCG stellar mass estimates derived from photometry (M_{*}^{BCG}) and from spectroscopy by Chen et al. (2012) (M_{*}^{Wisc}). Each galaxy is colour-coded by the stellar age of the SSP inferred by EzGal, according to the colour bar on the right. Our stellar mass estimates are systematically lower than the Chen et al. (2012) values by 0.1–0.15 dex, indicating by the black solid line that goes through the median logarithmic M_{*}^{BCG} at fixed M_{*}^{Wisc} (circles). This systematic shift is largely caused by the different assumptions in the adopted SSP and IMF models, as well as the different apertures assumed in the two measurements.

There is also a scatter of ~ 0.07 dex (errorbars on the circles)

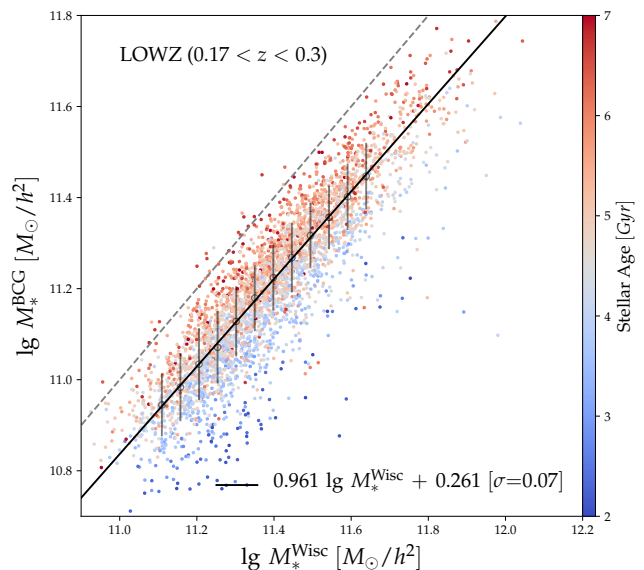


Figure 1. Comparison of the BCG stellar mass estimates derived from spectroscopy and photometry, for the redMaPPer BCGs that have spectra from the BOSS LOWZ galaxy sample within $z=0.17$ and 0.3 . The stellar age of each BCG, colour-coded by the colour bar on the right, is estimated from the photometric modelling. Black circles are the median stellar mass estimated from photometry at fixed spectroscopically-measured stellar mass, with the error bars indicating the standard deviation. Black solid line is the linear fit to the median relation between the two logarithmic stellar mass estimates. Gray dashed line shows the one-to-one line for reference.

between the EzGal and Chen et al. (2012) masses, mainly due to the differences in the assumed star formation histories (SFHs). Our choice of SFH being a single burst is likely too simplified to describe some of the colour deviations from predicted by a passively-evolving stellar population of a single age, producing a degeneracy between the inferred stellar mass and age. Since this extra age-induced scatter is only one third of the total scatter of M_{*}^{BCG} at fixed λ (0.21 dex; see Figure 2), it is unlikely that the lensing discrepancies (as we will observe later in §4) between the high and low- M_{*}^{BCG} subsamples are caused by the systematic uncertainties in the assumed SFH. Interestingly, Montero-Dorta et al. (2017); Niemiec et al. (2018) detected significant clustering difference between the luminous red galaxies split by their SFH, which could be an indication of the galaxy assembly bias, but at a much higher redshift ($z \sim 5$) and for lower mass systems ($\sim 8 \times 10^{12} h^{-1} M_{\odot}$) than our sample.

2.3 Low and High- M_{*}^{BCG} Cluster Subsamples

Equipped with the homogeneous stellar mass estimates for all 4567 BCGs in our cluster sample, we now divide them into subsamples of different average M_{*}^{BCG} but the same average halo mass. To make sure the signal-to-noise of the weak lensing measurement of each subsample is high enough for inferring halo mass and concentration, we do not sub-divide the clusters into smaller bins in λ , but introduce a λ -dependent stellar mass cut to separate the clusters into two equal-size subsamples with the same distributions of λ . Since λ is an excellent proxy of halo mass with a tight scatter (Roza & Rykoff 2014), we are hopeful that the two cluster subsamples have similar average halo masses, as will be seen in §4. Similar sliding

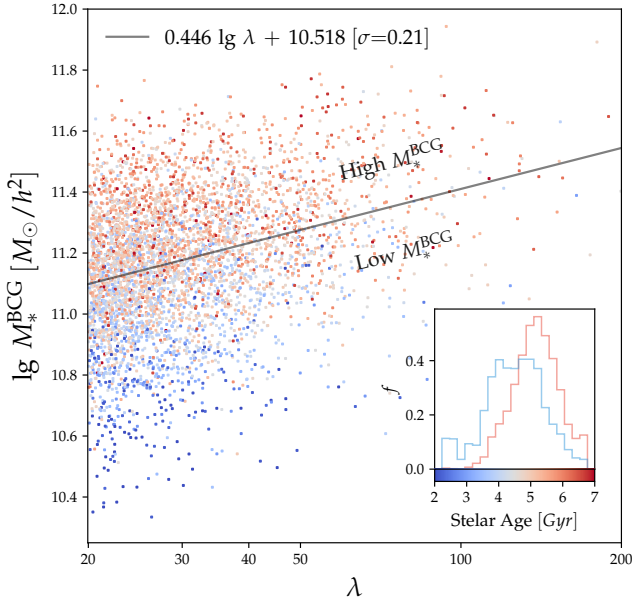


Figure 2. Distribution of clusters on the BCG stellar mass vs. satellite richness plane, each colour-coded according to their BCG stellar ages by the colour bar underneath the inset panel. The black line is a linear fit to the running median of the logarithmic stellar mass at fixed richness, described by the equation on the top left. The cluster sample is split into two halves with the same richness distribution but different average BCG stellar masses by the black line. The inset panel shows the stellar age distribution of the high (red) and low (blue) M_*^{BCG} subsamples. The average stellar age of the high- M_*^{BCG} subsample is higher than the low- M_*^{BCG} , but the two distributions have significant overlap around the median stellar age of the total sample.

cuts across the observable- λ plane was also adopted in other cluster assembly bias studies (Miyatake et al. 2016; Zu et al. 2017).

Figure 2 shows the distribution of clusters on the M_*^{BCG} vs. λ plane, with each cluster colour-coded by the stellar age of its BCG according to the colourbar underneath the inset panel. The gray line indicates the λ -dependent stellar mass cut that we adopt to divide the sample into low vs. high stellar mass halves. For the rest of the paper, we will refer to the two halves simply as “low” and “high”- M_*^{BCG} subsamples, despite that this is not a uniform stellar mass cut across different λ . The scatter of M_*^{BCG} at fixed λ about the mean M_*^{BCG} - λ relation, described by the parameters in the top left corner, is about 0.21 dex. If we assume that the additional scatter caused by the stellar age uncertainties is independent of the true scatter in the SHMR and subtract 0.07 dex from the quadrature, we arrive at a scatter in the M_*^{BCG} - λ relation of 0.20 dex, in excellent agreement with spectroscopic observations of the SHMR from, e.g., Zu & Mandelbaum (2015, 2016). The blue and red histograms in the inset panel of Figure 2 are the stellar age distributions of the low and high- M_*^{BCG} subsamples, respectively. There is a substantial overlap in the stellar age distributions of the two populations, indicating that any observed discrepancy between the two should primarily be linked to the difference in their average stellar masses instead of age. After the split, the difference in the average log-stellar mass between the two subsamples is about 0.34 dex (11.00 vs. 11.34).

2.4 Cluster Weak Lensing Measurements

We measure the weak gravitational lensing signals for the two cluster subsamples using two independent measurement methods with separate shear catalogues from two imaging surveys. We perform the first set of measurements by closely following the method presented in Simet et al. (2017). The shear catalogue was derived from SDSS images of DR8 (Reyes et al. 2012) using the re-Gaussianisation algorithm (Hirata & Seljak 2003) and the photometric redshifts of the source catalogue were calculated using the Zurich Extragalactic Bayesian Redshift Analyzer (ZEBRA Feldmann et al. 2006). Further characterization of the systematic errors and shear calibrations can be found in Mandelbaum et al. (2012, 2013), while the impact of photo- z errors on the weak lensing measurements can be found in Nakajima et al. (2012). We refer readers to Simet et al. (2017) for technical details of this cluster weak lensing measurement based on the SDSS shear catalogue.

We also perform a second set of weak lensing measurements using the shear catalogue derived from the DECaLS images of DR8 (Dark Energy Camera Legacy Survey; Dey et al. 2019), using the photometric redshift estimates from Zou et al. (2019) via the K-Nearest-Neighbour (KNN) method. The sources from the *Tractor* catalogue (Lang et al. 2014) are divided into five morphological types: Point sources (PSF), round exponential galaxies with a variable radius (REX), DeVaucouleurs (DEV), Exponential (EXP), and Composite model (COMP). Sources above 6σ detection limit in any stack are kept as candidates. PSF and REX models are adjusted on individual images convolved by their own PSF model. Galaxy ellipticities, which are free parameters of the above four REX, DEV, EXP and COMP models, are estimated by a joint fit on the three optical grz bands. We model potential measurement biases with a multiplicative and an additive bias (e.g., Heymans et al. 2012; Miller et al. 2013). The multiplicative bias comes from the shear measurement and imperfect modeling of PSF size. In order to calibrate our shear catalogue, we cross-matched the DECaLS DR8 objects with the external shear measurements, including Canada-France-Hawaii Telescope (CFHT) Stripe 82 (Morales et al. 2014), Dark Energy Survey (Dark Energy Survey Collaboration et al. 2016, DES;), and Kilo-Degree Survey (Hildebrandt et al. 2017, KiDS;), and then computed the correction parameters (Phriksee et al. 2020). The additive bias is expected to come from residuals in the anisotropic PSF correction, which depends on galaxy sizes. The additive bias is subtracted from each galaxy in the catalogue. The same shear catalogue and photo- z measurements (but from DECaLS DR3) were used in the weak lensing analysis of CODEX clusters by Phriksee et al. (2020) and the intrinsic alignment studies of Yao et al. (2020), and we refer readers to these two papers for technical details of the DECaLS shear catalogue and KNN photo- z errors.

Since DECaLS is roughly 1.5 to 2 magnitudes deeper than SDSS in the r -band, the effective source number density is higher in DECaLS (1.8 arcmin^{-2}), about five times larger than in SDSS², while the typical shape noise in DECaLS (0.23) is slightly higher than in SDSS (0.21). Therefore, we expect the uncertainties in the DECaLS weak lensing signal to be smaller by about a factor of two compared to the SDSS ($\sqrt{5} \times (0.21/0.23)$) for the same area coverage (the effective source areas of our DECaLS and SDSS measurements are both 9000 deg^2). For both measurements in SDSS and DECaLS, we employ the same prescription as outlined in Mandelbaum et al. (2005, 2013) to apply the “boost factor”, to

² We have included the critical surface density Σ_c weighting in the calculation of effective source number densities.

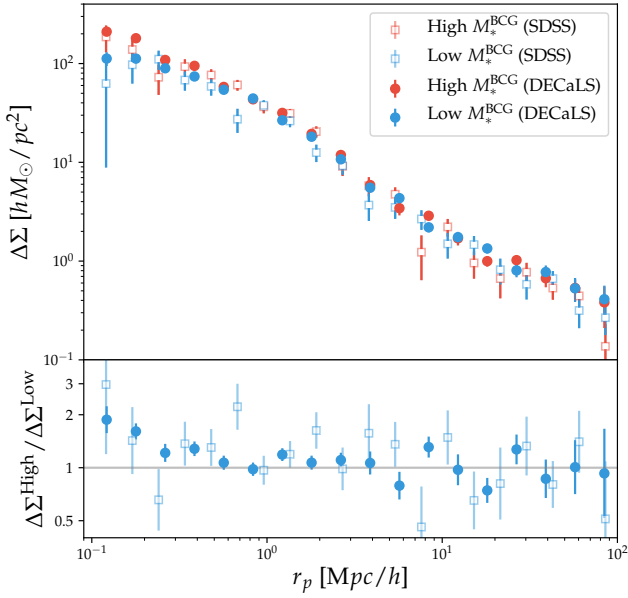


Figure 3. *Top:* Surface density contrast profiles of the low (blue) and high (red) M_*^{BCG} subsamples, measured from the SDSS (open squares with errorbars) and DECaLS (solid circles with errorbars) source catalogues. The smaller uncertainties in the DECaLS measurements are mainly due to the higher effective number of sources in DECaLS than in SDSS. *Bottom:* The ratio between the $\Delta\Sigma$ profiles of the high and low- M_*^{BCG} subsamples derived from SDSS (open squares) and DECaLS (filled circles).

correct for the fact that the lensing signal is diluted by the inclusion of sources that are physically associated with the lens (therefore not really lensed). We derive the uncertainties of both sets of cluster weak lensing measurements using the Jackknife resampling method, by dividing the sample footprint into 200 contiguous regions of the same area.

The top panel of Figure 3 shows the cluster weak lensing measurements of the low (blue) and high (red) M_*^{BCG} subsamples. Open squares and filled circles are the surface density contrast ($\Delta\Sigma$) profiles measured from SDSS and DECaLS shear catalogues, respectively. For each subsample, the two sets of shear catalogues yield consistent $\Delta\Sigma$ profiles. As expected, the uncertainties in the DECaLS measurements are smaller than SDSS by a factor of ~ 2 , consistent with our expectation. Focusing on the DECaLS measurements with smaller errorbars, we find that the two subsamples share similar $\Delta\Sigma$ profiles at projected distances above $1h^{-1}\text{Mpc}$; The two $\Delta\Sigma$ profiles start to differ below $r_p \sim 1h^{-1}\text{Mpc}$, with the high- M_*^{BCG} subsample showing a much steeper increase toward smaller scales than the low- M_*^{BCG} subsample, which shows a flattening profile into the inner $100h^{-1}\text{kpc}$. This discrepancy on small scales can be seen more clearly in the bottom panel of Figure 3, where we show the ratio of the high and low- M_*^{BCG} $\Delta\Sigma$ profiles from SDSS (open squares) and DECaLS (filled circles) measurements. The SDSS measurements display very similar behaviors in the ratio profile, albeit with much larger uncertainties.

For the small-scale $\Delta\Sigma$ discrepancy, it is very tempting to interpret it as the manifestation of different halo concentrations at fixed average halo mass, hence a strong indication that the scatter in the BCG stellar mass is driven by concentration. However, unlike the X-ray images of clusters that always have prominent centroids of

emission, clusters in the optical do not necessarily have a dominant BCG in the center. Therefore, a fraction of the BCGs identified by the optical cluster finder could be incorrect, showing offsets from the X-ray centres, which are generally believed to be better aligned with the barycentres of the haloes (Johnston et al. 2007; George et al. 2012; Hollowood et al. 2019). Such a miscentring effect could play an important role in the interpretation of cluster weak lensing signals on scales up to $1h^{-1}\text{Mpc}$. Miscentring also adds extra scatter to the BCG stellar masses by replacing the stellar mass of the true BCG with that of the incorrect central galaxy. This extra scatter is less problematic because we can safely assume that the stellar mass of the true BCG is comparable to that of the miscentred galaxies, because the otherwise dominant true BCG would have been correctly identified by the centroiding algorithm. To distinguish between miscentring and concentration effects, and to ascertain whether the average halo masses are indeed similar, we will derive statistical constraints on halo mass, miscentring, and concentration by modelling the $\Delta\Sigma$ profiles measured from DECaLS imaging in the next section.

3 BAYESIAN INFERENCE OF CLUSTER PROPERTIES

3.1 Theoretical Modelling of $\Delta\Sigma$

We adopt a Bayesian framework for inferring the cluster density profiles from weak lensing signals. The surface density contrast profile $\Delta\Sigma$ can be computed as

$$\Delta\Sigma(r_p) = \bar{\Sigma}(\langle r_p \rangle) - \Sigma(r_p), \quad (1)$$

where $\bar{\Sigma}(\langle r_p \rangle)$ and $\Sigma(r_p)$ are the average surface matter density interior to and at radius r_p , respectively. In the absence of miscentring, $\Sigma(r_p)$ can be directly computed from the 3D isotropic halo-mass cross-correlation function $\xi_{\text{hm}}(r)$,

$$\Sigma(r_p) = \rho_m \int_{-\infty}^{+\infty} \xi_{\text{hm}}(r_p, r\pi) dr\pi, \quad (2)$$

where ρ_m is the mean density of the Universe. In practice, we ignore the effects of the broad lensing window function, and use $\pm 100h^{-1}\text{Mpc}$ for the integration limit.

To model the miscentring effect, we assume that the fraction of BCGs miscentred is f_{off} and their offsets r_{off} from the true centres follow a shape-2 Gamma distribution $p(r_{\text{off}})$ with a characteristic offset σ_{off} ,

$$p(r_{\text{off}}) = \frac{r_{\text{off}}}{\sigma_{\text{off}}^2} \exp\left(-\frac{r_{\text{off}}}{\sigma_{\text{off}}}\right). \quad (3)$$

The observed surface matter density in the presence of miscentring is thus

$$\Sigma^{\text{obs}}(r_p) = f_{\text{off}} \Sigma^{\text{off}}(r_p) + (1 - f_{\text{off}}) \Sigma(r_p), \quad (4)$$

where

$$\Sigma^{\text{off}}(r_p) = \frac{1}{2\pi} \int_0^\infty dr_{\text{off}} p(r_{\text{off}}) \int_0^{2\pi} d\theta \Sigma\left(\sqrt{r_p^2 + r_{\text{off}}^2 - 2r_p r_{\text{off}} \cos\theta}\right). \quad (5)$$

Finally, to calculate $\Sigma(r_p)$, we need to build an accurate model for ξ_{hm} on radial scales between $0.1h^{-1}\text{Mpc}$ and $\sim 100h^{-1}\text{Mpc}$. We adopt the two-component model of ξ_{hm} developed by Zu et al.

(2014) (a modified version proposed by Hayashi & White 2008),

$$\begin{aligned}\xi_{\text{hm}}(r) &= \begin{cases} \xi_{1\text{h}} & \text{if } \xi_{1\text{h}} \geq \xi_{2\text{h}}, \\ \xi_{2\text{h}} & \text{if } \xi_{1\text{h}} < \xi_{2\text{h}}, \end{cases} \\ \xi_{1\text{h}} &= \frac{\rho_{\text{NFW}}(r|M_h)}{\rho_{\text{m}}} - 1, \\ \xi_{2\text{h}} &= b \xi_{\text{mm}}.\end{aligned}\quad (6)$$

Here $\xi_{1\text{h}}$ and $\xi_{2\text{h}}$ are the so-called ‘‘1-halo’’ and ‘‘2-halo’’ terms in the halo model (Cooray & Sheth 2002), $\rho_{\text{NFW}}(r|M_h, c)$ is the NFW density profile of halo mass M_h and concentration c , b is the average halo bias, and ξ_{mm} is the non-linear matter-matter auto-correlation function predicted at *Planck* cosmology (Takahashi et al. 2012). Zu et al. (2014) found that this simple model provides an adequate description of the halo-matter cross-correlation measured from simulations at the level of a few per cent on scales of our concern (i.e., below the halo radius). For massive haloes, several studies found that the average density profile in the inner region of haloes deviates from the NFW shape and the Einasto profile is more accurate (Dutton & Macciò 2014; Klypin et al. 2016). However, since we are only fitting to scales above $0.1h^{-1}\text{Mpc}$, the difference between NFW and Einasto should be negligible. We have also ignored the extra lensing effect caused by the stellar mass of the BCGs, which has negligible contribution on scales above $0.1h^{-1}\text{Mpc}$. The uncertainties of the predicted $\Delta\Sigma$ can be as large as 10% around the transition between the 1-halo and 2-halo scales ($2\text{--}4h^{-1}\text{Mpc}$; see the figure 5 of Zu et al. 2014), but we are only concerned with the measurement of halo mass and concentration, which are inferred primarily from scales below the transition scale, and the large-scale bias, which is estimated from scales above $10h^{-1}\text{Mpc}$. Additionally, our statistical uncertainties of weak lensing at those scales is around 10%. Therefore, the impact of relatively large uncertainties in the transitional regime on our conclusions should be negligible. For future modelling of cluster weak lensing signals of per cent level uncertainties, the transitional behavior can be potentially improved by using the scheme proposed by Garcia et al. (2020) and emulators developed by Salcedo et al. (2020).

3.2 Model Priors and Likelihood

For each cluster subsample, we have five parameters for modelling the $\Delta\Sigma$ profile: three of them for describing ξ_{hm} (M_h , c , b) and two for miscentring (f_{off} , σ_{off}). The miscentring effect is highly degenerate with halo concentration if σ_{off} is allowed to vary arbitrarily. To mitigate such degeneracy in our constraint, we apply the results from the state-of-the-art calibration of the redMaPPer cluster miscentring from Zhang et al. (2019) as our priors for modelling the miscentring. Using the X-ray observations from *Chandra*, their constraints on the average offset and the average miscentring fraction are (listed in their table 1) $\langle\sigma_{\text{off}}\rangle = 0.18 \pm 0.02h^{-1}\text{Mpc}$ and $\langle f_{\text{off}}\rangle = 0.3 \pm 0.04$, respectively.

However, the calibration in Zhang et al. (2019) was derived for the overall SDSS redMaPPer sample, which is not directly applicable to our cluster subsamples split by M_*^{BCG} . For example, for our high- M_*^{BCG} subsample it is reasonable to expect the miscentring fraction f_{off} to be lower than 0.3, because more massive redMaPPer BCGs are more likely to be the correct central galaxies, and vice versa for the low- M_*^{BCG} subsample. To correctly make use of the Zhang et al. (2019) constraints in our analysis, we fit the $\Delta\Sigma$ profiles of the low and high- M_*^{BCG} subsamples jointly as a single data vector with ten model parameters (five for each subsample). During the fit, we derive the average miscentring parameters $\langle\sigma_{\text{off}}\rangle$ and

Table 1. Posterior constraints of the model parameters for the two subsamples. The uncertainties are the 68% confidence regions derived from the 1D posterior probability distributions.

Subsample	$\lg M_h$	c	b	σ_{off}	f_{off}
Low- M_*^{BCG}	$14.24^{+0.02}_{-0.02}$	$5.87^{+0.77}_{-0.60}$	$2.91^{+0.26}_{-0.27}$	$0.23^{+0.02}_{-0.02}$	$0.37^{+0.07}_{-0.06}$
High- M_*^{BCG}	$14.24^{+0.02}_{-0.02}$	$6.95^{+0.78}_{-0.66}$	$2.59^{+0.21}_{-0.21}$	$0.21^{+0.02}_{-0.03}$	$0.20^{+0.07}_{-0.07}$

$\langle f_{\text{off}}\rangle$ for the overall cluster sample in each likelihood calculation, and apply the Zhang et al. (2019) constraints as Gaussian priors on those two quantities, so that $\langle\sigma_{\text{off}}\rangle \sim \mathcal{N}(0.18h^{-1}\text{Mpc}, 0.02^2)$ and $\langle f_{\text{off}}\rangle \sim \mathcal{N}(0.3, 0.04^2)$, respectively. In this way, we implement the miscentring priors in our analysis self-consistently and correctly take into account the covariance between the two sets of $\Delta\Sigma$ parameters during the fit.

The concentration of a typical halo with $\lg M_h = 2 \times 10^{14}h^{-1}M_{\odot}$ is predicted to be roughly five by the ΛCDM model at *Planck* cosmology, so we place a broad Gaussian prior of the average concentration of each subsample as $c \sim \mathcal{N}(5, 1.5^2)$. Note that the average concentration of our cluster sample may be significantly higher than five, due to the increasing scatter of the mass-richness relation toward the low- λ end (Murata et al. 2018). Since the c - m relation increases rapidly toward the low-mass end, the progressively large scatter will introduce a large number of low-mass haloes that usually have significantly higher concentrations into our cluster sample. Nonetheless, this prior tends to drive the concentration values of the two subsamples closer during the fit, and is thus a conservative choice given our purpose of looking for discrepancies in c . We assume flat priors for the other two parameters of ξ_{hm} .

We assume a Gaussian likelihood model and compute the likelihoods by comparing the predicted $\Delta\Sigma$ to the DECaLS measurements on scales between $0.1h^{-1}\text{Mpc}$ and $20.0h^{-1}\text{Mpc}$. To infer the joint posterior distribution of the ten parameters, we employ the affine invariant Markov Chain Monte Carlo (MCMC) ensemble sampler *emcee* (Foreman-Mackey et al. 2013). We run the MCMC sampler for 2,000,000 steps for each analysis to ensure its convergence, and derive the posterior constraints after a burn-in period of 500,000 steps. The median values and the 68 per cent confidence limits of the 1D posterior constraints are listed in Table 1, with one row for each cluster subsample.

4 CONSTRAINTS ON HALO PROPERTIES

The derived posterior constraints of our model parameters for the low (blue) and high (red) M_*^{BCG} subsamples are displayed in Figure 4. The diagonal panels show the 1D marginalised posterior distributions of each of the five parameters, and the contours in the off-diagonal panels are the 50% and 90% confidence regions for each of the parameter combinations within each subsample. Note that we do not show the parameter covariances between the two subsamples because they are either very weak ($\lg M_h$, c , b) or can be entirely explained by the priors on the overall miscentring (f_{off} , σ_{off}).

The halo mass constraints of the two subsamples are almost exactly the same ($\lg M_h = 14.24 \pm 0.02$), confirming our expectations that the two subsamples have the same average halo mass. Interestingly, the model yields a $\sim 12\%$ higher bias for the low- M_*^{BCG} subsample (2.91 ± 0.27) than the high- M_*^{BCG} one (2.59 ± 0.21). However, the biases are less well constrained due to the relatively

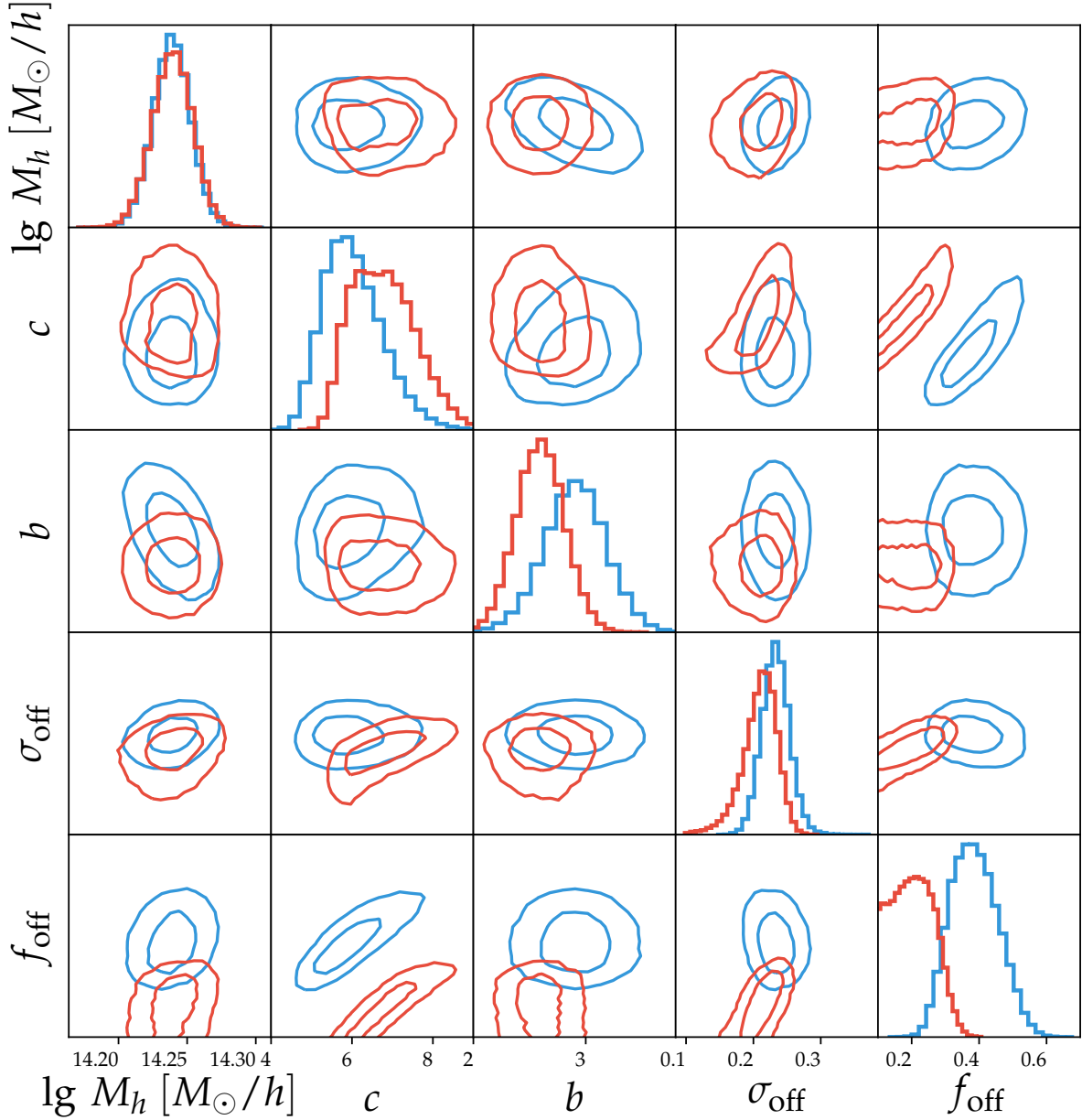


Figure 4. Posterior constraints from the modelling of $\Delta\Sigma$ of the low (blue) and high (red) M_*^{BCG} subsamples using the DECaLS imaging data. Each contour set in the off-diagonal panels indicate the 50% (inner contour) and 90% (outer contour) confidence regions of the matching parameter pair, and each histogram in the diagonal panels are the 1D marginalised posterior distribution of the respective parameter.

large uncertainties of $\Delta\Sigma$ on scales above $10h^{-1}\text{Mpc}$. We will examine the biases more closely in §5 using cross-correlations with galaxies. The characteristic offset of the high- M_*^{BCG} clusters ($0.21 \pm 0.02 h^{-1}\text{Mpc}$) is slightly smaller compared to the low- M_*^{BCG} subsample ($0.23 \pm 0.02 h^{-1}\text{Mpc}$), but their inferred miscentring fraction (0.20 ± 0.07) is lower than that of the low- M_*^{BCG} clusters (0.37 ± 0.07) by $\sim 1.5\sigma$. This indicates that the high- M_*^{BCG} clusters are indeed better centered than their low- M_*^{BCG} counterparts, and some of the small-scale discrepancies between the two $\Delta\Sigma$ profiles are due to a stronger miscentring effect in the low- M_*^{BCG} subsample.

As expected from §3.2, the concentration values inferred for

both subsamples are higher than five, the predicted value for a halo with $\lg M_h \approx 14.2$ in ΛCDM , likely due to the contribution from a large number of intrinsically low-mass haloes with much higher concentration. The average concentration of the overall cluster sample is $\sim 5-7$, consistent with the concentration measurements from Shan et al. (2017) and Simet et al. (2017).

After marginalising over the uncertainties in the miscentring, the two 1D posterior constraints on the halo concentrations exhibit a statistically significant difference ($>1\sigma$), with the low- M_*^{BCG} clusters having a lower concentration ($5.87^{+0.77}_{-0.60}$) than the high- M_*^{BCG} counterparts ($6.95^{+0.78}_{-0.66}$). For the discrepancy in the small-scale weak lensing signals to be entirely attributed to the difference in

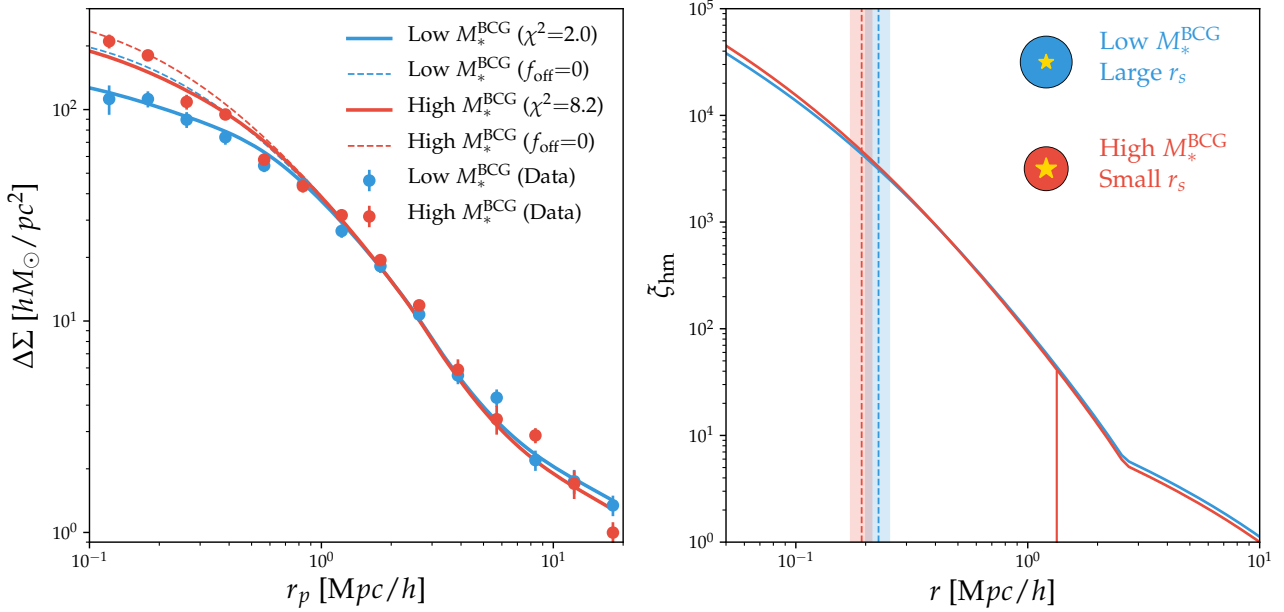


Figure 5. *Left panel:* Comparison between the $\Delta\Sigma$ predicted by the posterior mean models (thick solid curves) and the DECaLS measurements (circles with errorbars), for the low (blue) and high (red) M_*^{BCG} subsamples, respectively. The χ^2 values of the two posterior mean models are shown in the parentheses. Thin dashed curves of the matching colours indicate the model predictions in the absence of miscentering. *Right panel:* Comparison of the halo-matter cross-correlation functions between the low (blue) and high (red) M_*^{BCG} subsamples, inferred from the posterior mean models of the $\Delta\Sigma$ analysis (Equation 6). Blue and red vertical lines underneath the ξ_{hm} curves at $r \approx 1.33h^{-1}\text{Mpc}$ indicate the best-fitting r_{200m} of the low and high- M_*^{BCG} subsample, respectively, while the blue and red shaded vertical bands indicate the $1-\sigma$ ranges of characteristic radii r_s of the two corresponding best-fitting NFW profiles. The r_{200m} lines are almost indistinguishable because the inferred halo masses are similar, while the two r_s values differ by $\sim 20\%$. The two filled circles illustrate the size difference between the two r_s in linear scale, with the gold stars in the center representing the different average BCG stellar masses.

miscentering, the ratio of two miscentering fractions has to exceed $\sim 4:1$, which is mathematically plausible but highly unlikely. The concentration of the low- M_*^{BCG} subsample is roughly consistent with the input Gaussian prior on concentration. For the high- M_*^{BCG} subsample, it requires a miscentering fraction f_{off} of almost zero to reach the average concentration of the low- M_*^{BCG} subsample (5.87), and a negative f_{off} (i.e., unphysical) to be consistent with the prior.

Therefore, we believe the inferred high concentration of the high- M_*^{BCG} clusters is caused by the preference of massive BCGs to live in more concentrated haloes. Given that the two subsamples have the same average halo mass but differ significantly in their BCG stellar mass, our result here suggests that the dark matter concentration is indeed strongly tied to the stellar mass of the central galaxy in massive haloes. Since the concentration of a halo was set at the very early stage of halo formation, it is more likely that concentration drives the scatter in the SHMR of clusters, rather than vice versa.

Linking the discrepancies in both concentration and bias between the two subsamples, our results indicate that the low- M_*^{BCG} clusters are less concentrated on small scales but more clustered on large-scales than their high- M_*^{BCG} counterparts of the same halo mass. This observed secondary dependence of halo bias on concentration at fixed halo mass, if confirmed by more accurate measurements of bias, provides direct evidence for the existence of cluster assembly bias (Gao et al. 2005; Jing et al. 2007). We will return to the assembly bias discussion in §5.

Our inferred concentration- M_*^{BCG} connection and the evidence of halo assembly bias point to a simple yet remarkable picture of cluster formation across distance scales of three orders of magnitudes, from the stellar mass within tens of $k\text{pc}$, to dark matter density

within the scale radius of hundreds of $k\text{pc}$, and finally to the large-scale overdensity of cluster haloes on several tens of Mpc . In this picture, at fixed cluster mass and richness, the highly concentrated haloes host more massive galaxies in the center, but preferentially live in lower-density large-scale environments.

The left panel of Figure 5 compares the $\Delta\Sigma$ predicted by the posterior mean models (thick solid curves) to the DECaLS observations (circles with errorbars), for the low (blue) and high (red) M_*^{BCG} subsamples. The high- M_*^{BCG} observations are slightly higher than predicted on scales below $0.2h^{-1}\text{Mpc}$, probably due to some unknown deviations from our simple miscentering model or underestimated systematic uncertainties in the small-scale weak lensing measurements. Overall, the model predictions provide a very good overall description to the data points on all scales for both subsamples. We also show the two model predictions assuming there is no miscentering with the thin dashed curves, by setting $f_{\text{off}}=0$ while keeping all other parameters fixed to the posterior mean values. Clearly, miscentering incurs a much larger suppression in the weak lensing signals of the low- M_*^{BCG} subsample (blue dashed thin curve) than that of the high- M_*^{BCG} subsample (red dashed thin curve) on smaller scales. Nevertheless, the model predicts that approximately half of the observed small-scale discrepancy in $\Delta\Sigma$ is induced by the intrinsic difference in their average halo concentrations.

On the right panel of Figure 5, we illustrate the two corresponding ξ_{hm} profiles predicted by the posterior mean models for the low (blue) and high (red) M_*^{BCG} subsamples. The corresponding vertical lines underneath the ξ_{hm} curves indicate the predicted r_{200m} , which are indistinguishable between the two subsamples. The blue and red shaded vertical bands indicate the $1-\sigma$ ranges of

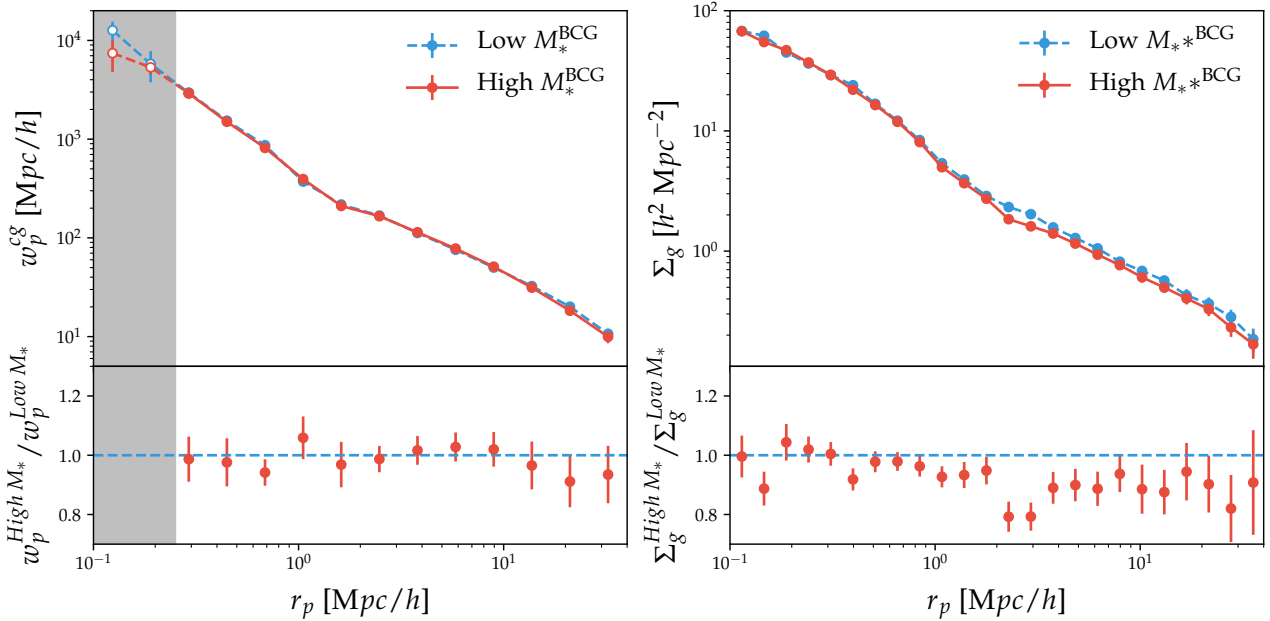


Figure 6. *Left panel:* Comparison of the projected correlation functions of the low (blue) and high (red) M_*^{BCG} subsamples with the BOSS LOWZ spectroscopic galaxy sample in the upper subpanel, with the ratio of the two shown in the bottom subpanel. The gray shaded region on the left indicates the distance scales that are affected by the fibre collision in BOSS. *Right panel:* Similar to the left panel, but for the excess galaxy surface number density profile calculated from the SDSS DR8 imaging. In both panels, the two profiles are consistent on scales below $1h^{-1}\text{Mpc}$, confirming that the satellite richnesses of the two subsamples are the same; The low- M_*^{BCG} subsample has a slightly higher clustering bias than the high- M_*^{BCG} subsample on scales above $10h^{-1}\text{Mpc}$, consistent with the weak lensing analysis.

the two characteristic scale radii r_s of the low and high- M_*^{BCG} subsamples, respectively. In a more visually appealing way, the blue and red filled circles in the top right corner compare the relative sizes of the two r_s values in linear proportion, and the stars in the center roughly illustrate the different average stellar masses of the central galaxies — at fixed halo mass, more concentrated clusters have more massive central galaxies.

Therefore, our weak lensing analysis suggests that the two cluster subsamples, divided by their BCG stellar masses, have very similar average halo masses, but likely differ in their concentration parameters by $\sim 18\%$. The simplest explanation is that, the halo concentration parameter is the key driver in setting the stellar mass of the BCGs in massive clusters. Intriguingly, the concentration-stellar mass relation at fixed halo mass is also directly linked to the halo bias, which we further investigate in the next section using cluster-galaxy cross-correlations.

5 CLUSTER ASSEMBLY BIAS FROM CROSS-CORRELATIONS WITH GALAXIES

From the weak lensing analysis, we find that the two cluster subsamples split by M_*^{BCG} have very similar average halo masses, but differ in their concentrations after marginalising over the degeneracy between concentration and miscentring effects. Additionally, the weak lensing analysis also suggests that the two subsamples differ in halo bias, a possible manifestation of the cluster assembly bias effect that has yet to be detected (Miyatake et al. 2016; Zu et al. 2017).

To further investigate whether the two subsamples have different halo bias, we measure their projected cross-correlation functions with BOSS LOWZ spectroscopic (w_p^{cg}) and SDSS photometric galaxies (Σ_g), shown in the left and right panels of Figure 6, re-

spectively. In each panel, blue and red circles with errorbars are the measurements for the low and high- M_*^{BCG} subsamples, respectively, and circles with errorbars in the bottom subpanel show the ratios between the high and low- M_*^{BCG} measurements. The error matrices are estimated from the same Jackknife resampling technique as in the cluster weak lensing measurements. The gray shaded band in the left panel indicates the scales affected by the fibre collision in BOSS. For the sake of brevity, we directly present the measurement results in this paper without the technical details, as we are only concerned with the relative difference between the large-scale clustering of the two subsamples. We faithfully follow Zu (2020) for the LOWZ galaxy sample selection and the w_p calculation, while the SDSS imaging galaxies and the calculation of surface number density profile Σ_g can be found in More et al. (2016).

Clearly, the two sets of measurements in Figure 6 are consistent with our results from the weak lensing analysis. That is, the low- M_*^{BCG} cluster subsample has a $\sim 10\%$ higher large-scale clustering than their high- M_*^{BCG} counterparts on scales larger than $10h^{-1}\text{Mpc}$. The bias discrepancy is around 1σ for w_p^{cg} , and close to 1.5σ for Σ_g . The two projected spectroscopic correlation functions w_p^{cg} start to differ at $\sim 10h^{-1}\text{Mpc}$, while the two photometric galaxy number density profiles Σ_g bifurcate on much smaller scales ($2h^{-1}\text{Mpc}$), probably because the photometric signal is dominated by galaxies that are much fainter than the LOWZ galaxies and have a different scale-dependent assembly bias. On scales below $1h^{-1}\text{Mpc}$, the two subsample shows very similar galaxy correlation signals, which is by design because they have the same satellite richness and similar weak lensing halo masses.

It is interesting if the cross-correlations with galaxies shown in Figure 6 would show any evidence of difference in the galaxy concentrations on small scales. For w_p^{cg} , unfortunately the fibre

collision scale is comparable to the r_s inferred from weak lensing, preventing any meaningful measurement of galaxy concentration. The cluster cross-correlations with photometric galaxies are free of fibre collision, and indeed exhibit a weak evidence that the satellite galaxies in the high- M_*^{BCG} clusters are slightly more concentrated than those in the low- M_*^{BCG} systems on scales below $1h^{-1}\text{Mpc}$. However, the uncertainties are too large to make a more concrete statistical statement.

To summarise, the cluster-galaxy cross-correlation functions provide further support of our conclusion from the weak lensing analysis, that the large-scale bias of the low- M_*^{BCG} , low- c clusters is 10% higher than that of their high- M_*^{BCG} , high- c counterparts with the same average halo mass. The *physical* connection of the three key cluster properties across scales of almost three orders of magnitudes, the stellar content within $20\text{--}30h^{-1}\text{kpc}$, the dark matter density within $\sim 200h^{-1}\text{kpc}$, and the cosmic overdensity on scales above $10h^{-1}\text{Mpc}$, is remarkable, revealing a surprisingly elegant picture of the co-evolution of massive dark matter haloes and their central galaxies amid the hierarchical structure formation of our Universe.

6 A CONUNDRUM: DOES HALO MASS DEPEND ON M_*^{BCG} AT FIXED λ ?

Before concluding our work, we would like to briefly discuss an apparent halo mass conundrum in our result — the average halo masses of the low and high- M_*^{BCG} cluster subsamples are indistinguishable, despite the SHMR predicts that the average halo mass of the high- M_*^{BCG} clusters should be higher (e.g., see figure 11 of [Zu & Mandelbaum 2015](#)). In particular, since there is a ~ 0.25 dex scatter between our mass proxy λ and the true halo mass, the halo mass distribution at fixed λ should be fairly broad, especially at the low- λ end (see figure 7 of [Murata et al. 2018](#)). Naively, one might expect that the SHMR would still operate at fixed λ , so that the more massive BCGs would preferentially live in high-mass haloes than the less massive systems, creating a mass discrepancy around 0.2–0.3 dex between the two subsamples based on their 0.34 dex difference in average stellar mass. However, our weak lensing analysis indicates that the mass discrepancy, if exists at all, should be smaller than 0.04 dex, i.e., 10%.

In addition, the large-scale bias of the low- M_*^{BCG} subsample is 10% higher than that of the high- M_*^{BCG} subsample, further indicating that the halo mass of the high- M_*^{BCG} subsample is unlikely larger than that of the low- M_*^{BCG} one. The reason is as follows. The average halo bias increases steeply with halo mass above the characteristic nonlinear mass scale, and for haloes of $\lg M_h \simeq 14.2$ at the mean redshift of our sample, the slope $d \ln b / d \ln M_h$ is about 0.42. Therefore, a 0.2–0.3 dex halo mass enhancement in the high- M_*^{BCG} subsample would lead to a 20–30% higher bias of the high- M_*^{BCG} subsample than the low- M_*^{BCG} one (in the absence of halo assembly bias), yet we observe a 10% lower bias of the high- M_*^{BCG} subsample, i.e., a 30–40% bias inversion.

This strong bias inversion can not be entirely explained by halo assembly bias, if the halo mass of the high- M_*^{BCG} clusters were indeed 0.2–0.3 dex higher than their low- M_*^{BCG} counterparts. [Jing et al. \(2007\)](#) predicted that the bias of the 20% most concentrated haloes is 20% lower than the 20% least concentrated haloes in the cluster regime. Therefore, even if we assume an extreme scenario in which the low and high- M_*^{BCG} clusters correspond to the 20% least and most concentrated haloes, respectively, the halo assembly

bias effect would not be able to resolve the large bias inversion we observed in the data.

This is very intriguing. One possible explanation is that the stellar mass of the BCG correlates strongly with the satellite richness at any given halo mass, so that the halo mass distribution at fixed λ is non-trivially related to M_*^{BCG} . Evidence of such a correlation was recently suggested by [To et al. \(2020\)](#). In a future work ([Zu et al. in prep](#)), we will explore whether the correlation has to be positive or negative, and what halo mass dependence of the correlation is required to solve the conundrum we observed here.

Finally, we emphasize that the main conclusion of this paper, which is derived from the observed *average* properties of the two cluster subsamples, is independent of the solution to such a halo mass conundrum, as long as the two share the same weak lensing halo mass.

7 CONCLUSION

In this paper, we have investigated the origin of the scatter in the SHMR of SDSS redMaPPer clusters by examining the weak gravitational lensing signals of two cluster subsamples split by their BCG stellar mass at fixed richness. To overcome the spectroscopic incompleteness of the BCG sample, we derived a homogeneous measurement of the BCG stellar masses from the SDSS *gri* photometry using the accurate cluster photometric redshifts estimated by the redMaPPer. Finally, using the shear catalogue derived from the DECaLS and SDSS imaging, we obtained accurate cluster weak lensing profiles $\Delta\Sigma$ for the two subsamples, which exhibit strong discrepancies on small scales.

To interpret the discrepancies in $\Delta\Sigma$, we modelled the DECaLS $\Delta\Sigma$ profiles using the halo-matter cross-correlation prescription of [Zu et al. \(2014\)](#) (a variant modified from [Hayashi & White 2008](#)), and carefully took into account the cluster miscentring calibrations from [Zhang et al. \(2019\)](#). After marginalising over the uncertainties in miscentring, we found that the two subsamples of clusters have almost the same average halo mass $\lg M_h = 14.24 \pm 0.02$, but different average values of halo concentration. In particular, the low- M_*^{BCG} clusters are on average less concentrated ($c = 5.87^{+0.77}_{-0.66}$) than the high- M_*^{BCG} systems ($6.95^{+0.78}_{-0.66}$). Our results provide direct evidence that the scatter in the stellar mass of central galaxies at fixed halo mass is strongly tied to the dark matter concentration of clusters.

Furthermore, we found that the low- M_*^{BCG} , low- c clusters are more clustered on scales above $10h^{-1}\text{Mpc}$ than their high- M_*^{BCG} , high- c counterparts from the weak lensing analysis. This finding is corroborated by our cluster-galaxy cross-correlation measurements using both the SDSS LOWZ spectroscopic and DR8 photometric galaxy samples. We interpret this observed dependence of large-scale bias on halo concentration at fixed cluster mass as a possible detection of the halo assembly bias effect, consistent with the expectations from the ΛCDM simulations ([Gao et al. 2005](#); [Jing et al. 2007](#); [Zu et al. 2017](#)).

Combining our two key findings, we infer that there likely exists a *physical* connection among the three key cluster properties across scales of almost three orders of magnitudes, the stellar mass within $20\text{--}30h^{-1}\text{kpc}$, the dark matter mass within $\sim 200h^{-1}\text{kpc}$, and the cosmic overdensity on scales above $10h^{-1}\text{Mpc}$, for clusters of the same average halo mass. This remarkable connection links the origin of the scatter in the cluster SHMR to the physics of halo assembly bias, thereby revealing a powerfully simple picture of the massive

galaxy formation within the hierarchical structure formation in our Universe.

The main sources of systematic uncertainties in our analysis are the modelling of miscentring effect and the accuracy of stellar mass estimates. The miscentring modelling in our analysis can be immediately improved by applying the Zhang et al. (2019) calibration to the two cluster subsamples separately. However, the current number of clusters with high-resolution X-ray observations is rather limited, and the miscentring calibration will benefit greatly from the upcoming X-ray surveys like the eROSITA (Merloni et al. 2012) and improved cluster centroiding algorithms. Meanwhile, the stellar mass estimates can be significantly improved with the upcoming observations by DESI (DESI Collaboration et al. 2016) and PFS (Takada et al. 2014), which will eliminate the spectroscopic incompleteness of the low-mass BCGs with bluer colours.

Looking forward, current deep imaging surveys like the DES (Dark Energy Survey Collaboration et al. 2016), HSC (Aihara et al. 2018), and LSST (Rubin; Ivezić et al. 2019) on the ground and future space missions like the *WFIRST* (Roman; Spergel et al. 2013), *Euclid* (Laureijs et al. 2011), and *CSST* (Chinese Space Station Telescope; Gong et al. 2019) will provide superb photometry for the measurement of stellar mass profiles of massive central galaxies (Huang et al. 2020) and the weak gravitational lensing signals of their host dark matter halos (Mandelbaum 2018). Finally, our inferred picture of cluster formation connects the structure formation across scales of three orders of magnitudes, thereby providing a stringent test of the theories of co-evolution between massive clusters and their brightest central galaxies (Naab & Ostriker 2017; Pillepich et al. 2018).

ACKNOWLEDGEMENTS

We thank the anonymous referee for the many constructive suggestions that have greatly improved the manuscript, Rachel Mandelbaum for carefully reading through the manuscript, and Melanie Simet for helpful discussions. YZ acknowledges the support by the National Key Basic Research and Development Program of China (No. 2018YFA0404504), National Science Foundation of China (11621303, 11873038, 11890692), the science research grants from the China Manned Space Project (No. CMS-CSST-2021-A01, CMS-CSST-2021-B01), the National One-Thousand the National One-Thousand Youth Talent Program of China, and the SJTU start-up fund (No. WF220407220). WC acknowledges the support from the European Research Council under grant 670193. YZ thanks the inspiring discussions with Cathy Huang during his visits to the Zhangjiang Hi-Tech Park.

REFERENCES

- Aihara H., et al., 2011, *ApJS*, **193**, 29
Aihara H., et al., 2018, *PASJ*, **70**, S4
Artale M. C., Zehavi I., Contreras S., Norberg P., 2018, *MNRAS*, **480**, 3978
Ascasibar Y., Hoffman Y., Gottlöber S., 2007, *MNRAS*, **376**, 393
Barnes J. E., Hernquist L. E., 1991, *ApJ*, **370**, L65
Bellstedt S., et al., 2016, *MNRAS*, **460**, 2862
Bernardi M., Meert A., Sheth R. K., Vikram V., Huertas-Company M., Mei S., Shankar F., 2013, *MNRAS*, **436**, 697
Bertschinger E., 1985, *ApJS*, **58**, 39
Bezanson R., van Dokkum P. G., Tal T., Marchesini D., Kriek M., Franx M., Coppi P., 2009, *ApJ*, **697**, 1290
Bond J. R., Cole S., Efstathiou G., Kaiser N., 1991, *ApJ*, **379**, 440
Bose S., Eisenstein D. J., Hernquist L., Pillepich A., Nelson D., Marinacci F., Springel V., Vogelsberger M., 2019, *MNRAS*, **490**, 5693
Bower R. G., 1991, *MNRAS*, **248**, 332
Bruzual G., Charlot S., 2003, *MNRAS*, **344**, 1000
Bullock J. S., Kolatt T. S., Sigad Y., Somerville R. S., Kravtsov A. V., Klypin A. A., Primack J. R., Dekel A., 2001, *MNRAS*, **321**, 559
Chabrier G., 2003, *PASP*, **115**, 763
Chen Y.-M., et al., 2012, *MNRAS*, **421**, 314
Chen Y., Mo H. J., Li C., Wang H., Yang X., Zhang Y., Wang K., 2020, *ApJ*, **899**, 81
Collins C. A., et al., 2009, *Nature*, **458**, 603
Cooray A., Sheth R., 2002, *Phys. Rep.*, **372**, 1
Costanzi M., et al., 2019, *MNRAS*, **488**, 4779
Cui W., et al., 2018, *MNRAS*, **480**, 2898
DESI Collaboration et al., 2016, arXiv e-prints, p. arXiv:1611.00036
Dalal N., White M., Bond J. R., Shirokov A., 2008, *ApJ*, **687**, 12
Dalal N., Lithwick Y., Kuhlen M., 2010, arXiv e-prints, p. arXiv:1010.2539
Dark Energy Survey Collaboration et al., 2016, *MNRAS*, **460**, 1270
De Lucia G., Blaizot J., 2007, *MNRAS*, **375**, 2
DeMaio T., et al., 2020, *MNRAS*, **491**, 3751
Dey A., et al., 2019, *AJ*, **157**, 168
Diemer B., Kravtsov A. V., 2015, *ApJ*, **799**, 108
Dubinski J., 1998, *ApJ*, **502**, 141
Dutton A. A., Macciò A. V., 2014, *MNRAS*, **441**, 3359
Fabian A. C., 1994, *ARA&A*, **32**, 277
Feldmann R., et al., 2006, *MNRAS*, **372**, 565
Ferrarese L., Merritt D., 2000, *ApJ*, **539**, L9
Fillmore J. A., Goldreich P., 1984, *ApJ*, **281**, 1
Foreman-Mackey D., Hogg D. W., Lang D., Goodman J., 2013, *PASP*, **125**, 306
Gao L., Springel V., White S. D. M., 2005, *MNRAS*, **363**, L66
Gao L., Navarro J. F., Cole S., Frenk C. S., White S. D. M., Springel V., Jenkins A., Neto A. F., 2008, *MNRAS*, **387**, 536
Garcia R., Rozo E., Becker M. R., More S., 2020, arXiv e-prints, p. arXiv:2006.12751
Gebhardt K., et al., 2000, *ApJ*, **539**, L13
George M. R., et al., 2012, *ApJ*, **757**, 2
Golden-Marx J. B., Miller C. J., 2018, *ApJ*, **860**, 2
Golden-Marx J. B., Miller C. J., 2019, *ApJ*, **878**, 14
Gong Y., et al., 2019, *ApJ*, **883**, 203
Gültekin K., et al., 2009, *ApJ*, **698**, 198
Gunn J. E., Gott J. Richard I., 1972, *ApJ*, **176**, 1
Hayashi E., White S. D. M., 2008, *MNRAS*, **388**, 2
Hellwing W. A., Cautun M., van de Weygaert R., Jones B. T., 2020, arXiv e-prints, p. arXiv:2011.08840
Heymans C., et al., 2012, *MNRAS*, **427**, 146
Hikage C., Mandelbaum R., Leauthaud A., Rozo E., Rykoff E. S., 2018, *MNRAS*, **480**, 2689
Hildebrandt H., et al., 2017, *MNRAS*, **465**, 1454
Hilz M., Naab T., Ostriker J. P., 2013, *MNRAS*, **429**, 2924
Hirata C., Seljak U., 2003, *MNRAS*, **343**, 459
Hollowood D. L., et al., 2019, *ApJS*, **244**, 22
Hopkins P. F., Bundy K., Murray N., Quataert E., Lauer T. R., Ma C.-P., 2009, *MNRAS*, **398**, 898
Hopkins P. F., Cox T. J., Hernquist L., Narayanan D., Hayward C. C., Murray N., 2013, *MNRAS*, **430**, 1901
Huang S., Leauthaud A., Greene J. E., Bundy K., Lin Y.-T., Tanaka M., Miyazaki S., Komiyama Y., 2018, *MNRAS*, **475**, 3348
Huang S., et al., 2020, *MNRAS*, **492**, 3685
Ishiyama T., Prada F., Klypin A. A., Sinha M., Metcalf R. B., Jullo E., Altieri B., et al., 2020, arXiv, arXiv:2007.14720
Ivezić Z., et al., 2019, *ApJ*, **873**, 111
Jing Y. P., Suto Y., 2000, *ApJ*, **529**, L69
Jing Y. P., Suto Y., Mo H. J., 2007, *ApJ*, **657**, 664
Johnston D. E., et al., 2007, arXiv e-prints, p. arXiv:0709.1159
Klypin A. A., Trujillo-Gomez S., Primack J., 2011, *ApJ*, **740**, 102
Klypin A., Yepes G., Gottlöber S., Prada F., Heß S., 2016, *MNRAS*, **457**, 4340

- Kochanek C. S., White M., Huchra J., Macri L., Jarrett T. H., Schneider S. E., Mader J., 2003, *ApJ*, **585**, 161
- Koester B. P., et al., 2007, *ApJ*, **660**, 239
- Kravtsov A. V., Borgani S., 2012, *ARA&A*, **50**, 353
- Kravtsov A. V., Vikhlinin A., Nagai D., 2006, *ApJ*, **650**, 128
- Kravtsov A. V., Vikhlinin A. A., Meshcheryakov A. V., 2018, *Astronomy Letters*, **44**, 8
- Lacey C., Cole S., 1993, *MNRAS*, **262**, 627
- Lang P., et al., 2014, *ApJ*, **788**, 11
- Laureijs R., et al., 2011, arXiv e-prints, p. arXiv:1110.3193
- Lin Y.-T., Mohr J. J., 2004, *ApJ*, **617**, 879
- Ludlow A. D., et al., 2013, *MNRAS*, **432**, 1103
- Macciò A. V., Dutton A. A., van den Bosch F. C., 2008, *MNRAS*, **391**, 1940
- Mancone C. L., Gonzalez A. H., 2012, *PASP*, **124**, 606
- Mandelbaum R., 2018, *ARA&A*, **56**, 393
- Mandelbaum R., et al., 2005, *MNRAS*, **361**, 1287
- Mandelbaum R., Hirata C. M., Leauthaud A., Massey R. J., Rhodes J., 2012, *MNRAS*, **420**, 1518
- Mandelbaum R., Slosar A., Baldauf T., Seljak U., Hirata C. M., Nakajima R., Reyes R., Smith R. E., 2013, *MNRAS*, **432**, 1544
- Maraston C., Strömbäck G., Thomas D., Wake D. A., Nichol R. C., 2009, *MNRAS*, **394**, L107
- Martizzi D., Teyssier R., Moore B., 2012, *MNRAS*, **420**, 2859
- Matthee J., Schaye J., Crain R. A., Schaller M., Bower R., Theuns T., 2017, *MNRAS*, **465**, 2381
- McDonald M., et al., 2012, *Nature*, **488**, 349
- Merloni A., et al., 2012, arXiv e-prints, p. arXiv:1209.3114
- Mihos J. C., Hernquist L., 1996, *ApJ*, **464**, 641
- Miller L., et al., 2013, *MNRAS*, **429**, 2858
- Miyatake H., More S., Takada M., Spergel D. N., Mandelbaum R., Rykoff E. S., Rozo E., 2016, *Phys. Rev. Lett.*, **116**, 041301
- Mo H. J., White S. D. M., 1996, *MNRAS*, **282**, 347
- Montero-Dorta A. D., et al., 2017, *ApJ*, **848**, L2
- Moraes B., et al., 2014, in *Revista Mexicana de Astronomia y Astrofisica Conference Series*. pp 202–203
- More S., et al., 2016, *ApJ*, **825**, 39
- Mostoghiu R., Knebe A., Cui W., Pearce F. R., Yepes G., Power C., Dave R., Arth A., 2019, *MNRAS*, **483**, 3390
- Murata R., Nishimichi T., Takada M., Miyatake H., Shirasaki M., More S., Takahashi R., Osato K., 2018, *ApJ*, **854**, 120
- Naab T., Ostriker J. P., 2017, *ARA&A*, **55**, 59
- Naab T., Johansson P. H., Ostriker J. P., 2009, *ApJ*, **699**, L178
- Nakajima R., Mandelbaum R., Seljak U., Cohn J. D., Reyes R., Cool R., 2012, *MNRAS*, **420**, 3240
- Navarro J. F., Frenk C. S., White S. D. M., 1997, *ApJ*, **490**, 493
- Neto A. F., et al., 2007, *MNRAS*, **381**, 1450
- Niemiec A., et al., 2018, *MNRAS*, **477**, L1
- Oguri M., et al., 2018, *PASJ*, **70**, S20
- Phriksee A., Jullo E., Limousin M., Shan H., Finoguenov A., Komonjinda S., Wannawichian S., Sawangwit U., 2020, *MNRAS*, **491**, 1643
- Pillepich A., et al., 2018, *MNRAS*, **475**, 648
- Planck Collaboration et al., 2020, *A&A*, **641**, A6
- Prada F., Klypin A. A., Cuesta A. J., Betancort-Rijo J. E., Primack J., 2012, *MNRAS*, **423**, 3018
- Ragone-Figueroa C., Granato G. L., Ferraro M. E., Murante G., Biffi V., Borgani S., Planelles S., Rasia E., 2018, *MNRAS*, **479**, 1125
- Ragagnin A., Dolag K., Moscardini L., Biviano A., D’Onofrio M., 2019, *MNRAS*, **486**, 4001. doi:10.1093/mnras/stz1103
- Reid B., et al., 2016, *MNRAS*, **455**, 1553
- Rennehan D., Babul A., Hayward C. C., Bottrell C., Hani M. H., Chapman S. C., 2020, *MNRAS*, **493**, 4607
- Rey M. P., Pontzen A., Saintonge A., 2019, *MNRAS*, **485**, 1906
- Reyes R., Mandelbaum R., Gunn J. E., Nakajima R., Seljak U., Hirata C. M., 2012, *MNRAS*, **425**, 2610
- Roza E., Rykoff E. S., 2014, *ApJ*, **783**, 80. doi:10.1088/0004-637X/783/2/80
- Roza E., Rykoff E. S., Becker M., Reddick R. M., Wechsler R. H., 2015, *MNRAS*, **453**, 38
- Rudd D. H., Zentner A. R., Kravtsov A. V., 2008, *ApJ*, **672**, 19
- Rykoff E. S., et al., 2014, *ApJ*, **785**, 104
- Salcedo A. N., Wibking B. D., Weinberg D. H., Wu H.-Y., Ferrer D., Eisenstein D., Pinto P., 2020, *MNRAS*, **491**, 3061
- Salvador-Solé E., Solanes J. M., Manrique A., 1998, *ApJ*, **499**, 542
- Shan H., et al., 2017, *ApJ*, **840**, 104
- Sheth R. K., Tormen G., 1999, *MNRAS*, **308**, 119
- Simet M., McClintock T., Mandelbaum R., Roza E., Rykoff E., Sheldon E., Wechsler R. H., 2017, *MNRAS*, **466**, 3103
- Spergel D., et al., 2013, arXiv e-prints, p. arXiv:1305.5422
- Szabo T., Pierpaoli E., Dong F., Pipino A., Gunn J., 2011, *ApJ*, **736**, 21
- Takada M., et al., 2014, *PASJ*, **66**, R1
- Takahashi R., Sato M., Nishimichi T., Taruya A., Oguri M., 2012, *ApJ*, **761**, 152. doi:10.1088/0004-637X/761/2/152
- To C.-H., Reddick R. M., Roza E., Rykoff E., Wechsler R. H., 2020, *ApJ*, **897**, 15
- Tojeiro R., et al., 2017, *MNRAS*, **470**, 3720
- Von Der Linden A., Best P. N., Kauffmann G., White S. D. M., 2007, *MNRAS*, **379**, 867
- Wang L., De Lucia G., Weinmann S. M., 2013, *MNRAS*, **431**, 600
- Wang K., Mao Y.-Y., Zentner A. R., Lange J. U., van den Bosch F. C., Wechsler R. H., 2020a, *MNRAS*, **498**, 4450
- Wang J., Bose S., Frenk C. S., Gao L., Jenkins A., Springel V., White S. D. M., 2020b, *Nature*, **585**, 39
- Wechsler R. H., Tinker J. L., 2018, *ARA&A*, **56**, 435
- Wechsler R. H., Bullock J. S., Primack J. R., Kravtsov A. V., Dekel A., 2002, *ApJ*, **568**, 52
- Wen Z. L., Han J. L., Liu F. S., 2012, *ApJS*, **199**, 34
- Yao J., Shan H., Zhang P., Kneib J.-P., Jullo E., 2020, *ApJ*, **904**, 135
- York D. G., et al., 2000, *AJ*, **120**, 1579
- Zehavi I., Kerby S. E., Contreras S., Jiménez E., Padilla N., Baugh C. M., 2019, *ApJ*, **887**, 17
- Zhang Y., et al., 2016, *ApJ*, **816**, 98
- Zhang Y., et al., 2019, *MNRAS*, **487**, 2578
- Zhao D. H., Mo H. J., Jing Y. P., Börner G., 2003, *MNRAS*, **339**, 12
- Zhao D. H., Jing Y. P., Mo H. J., Börner G., 2009, *ApJ*, **707**, 354
- Zou H., Gao J., Zhou X., Kong X., 2019, *ApJS*, **242**, 8
- Zu Y., 2020, arXiv e-prints, p. arXiv:2010.01143
- Zu Y., Mandelbaum R., 2015, *MNRAS*, **454**, 1161
- Zu Y., Mandelbaum R., 2016, *MNRAS*, **457**, 4360
- Zu Y., Weinberg D. H., Roza E., Sheldon E. S., Tinker J. L., Becker M. R., 2014, *MNRAS*, **439**, 1628
- Zu Y., Mandelbaum R., Simet M., Roza E., Rykoff E. S., 2017, *MNRAS*, **470**, 551
- van Dokkum P. G., et al., 2010, *ApJ*, **709**, 1018
- van den Bosch F. C., 2017, *MNRAS*, **468**, 885

This paper has been typeset from a $\text{\TeX}/\text{\LaTeX}$ file prepared by the author.